

# Model-Free Optimal Voltage Phasor Regulation in Unbalanced Distribution Systems

Michael D. Sankur, Roel Dobbe, Alexandra von Meier, and Daniel B. Arnold

**Abstract**—The proliferation of voltage Phasor Measurement Units (PMUs) into electric power distribution grids presents new opportunities for utility operators to manage their systems more effectively. In particular, distribution-level PMUs can serve as proxy measurements for active and reactive power flows, thus alleviating the need for current transformer-based measurements for certain applications. In this work, we explore the use of distribution PMU measurements to optimally control line power flows without explicit measurements of these quantities and without *a priori* knowledge of the underlying distribution system topology. To do so, we extend a 2 dimensional Extremum Seeking (2D-ES) control paradigm to simultaneously manage Distributed Energy Resource (DER) active and reactive power contributions in unbalanced distribution systems. Simulation results show the ability of the proposed approach to virtually island different portions of a 3-phase unbalanced the network using DER injections while maintaining proper voltage magnitudes in the rest of the network.

**Index Terms**—Distributed energy resources, Voltage regulation, Model-free control, Optimal control, Virtual islanding, Microgrid

## I. INTRODUCTION

The proliferation of new types of sensors into the electric power distribution system is providing deeper insights into grid operation and is driving innovation around new paradigms for system management. Among these new sensing devices, distribution voltage phasor measurement units (PMUs) provide types of measurements that can enable novel uses for Distributed Energy Resources (DER) to provide system-level benefits with minimum utility expense. Distribution voltage PMUs are already emerging in the marketplace either as standalone units [1] or embedded within other system components [2], [3], [4]. These devices provide access to voltage magnitude and phase angle data, which can serve as a proxy for active and reactive power flows. Distribution voltage PMUs may represent an attractive choice for utilities to gain access to system line flows as these devices do not require the use of current transformers in order to collect *voltage* phase magnitude and phase angle measurements.

The use of distribution PMU technology to inform more advanced control applications already have started to appear in literature. The work of [5] proposed the use of synchronized voltage phase angle measurements to curtail over-generation of renewables. Additionally, the authors of [6] considered voltage

Michael D. Sankur and Daniel B. Arnold are with Lawrence Berkeley National Laboratory. Roel Dobbe and Alexandra von Meier are with the Electrical Engineering and Computer Science Department at U.C. Berkeley. This work was supported in part by the U.S. Department of Energy ARPA-E (DE-AR0000340) and Office of Energy Efficiency and Renewable Energy (DE-EE0008008 and DE-AC02-05CH11231).

angle thresholds as criteria to connect renewable generation. Both works refer to this control activity as “Angle Constrained Active Management”, or ACAM.

One emerging application for the use of distribution voltage PMUs is to serve as proxy measurements for active and reactive power flows. This data, coupled with new approaches to manage DER, could then in turn be used to enable a host of applications including power target tracking and virtual islanding.

Several works have emerged that consider more advanced methods for islanding portions of electric distribution grids. In [7], the authors consider a two-tiered control system for microgrid islanding, consisting of a centralized controller for the microgrid, and distributed controllers for DER. The authors’ approach considers system frequency and network voltage magnitude for microgrid stability and reconnection. The authors of [8] investigate autonomous operation of microgrids, the islanding process, and reconnection process. The authors propose a system to minimize voltage magnitude error and voltage angle error between the microgrid and the main grid in order to minimize transient effects when disconnecting and reconnecting a microgrid.

Many other approaches found in literature for controlling distribution grids formulate the decision making process as an optimization program, often referred to as an Optimal Power Flow (OPF) problem [9], [10], [11], [12]. An OPF framework allows for proper modeling of the network topology, impedances and control equipment, the incorporation of safety constraints, and the formulation of various objective functions that can reflect important operating objectives such as loss minimization and cost of generation or control action. However, there is sparse literature on strategies that aim to *directly control the voltage phasor in OPF formulations*. The work of [9] proposes a distributed control framework to enable DER to track single-phase AC optimal power flow solutions using the Alternating Direction Method of Multipliers (ADMM). The authors of [10] consider a multi-timescale stochastic volt/var control method capable of controlling legacy voltage regulation systems as well as DER. Some of the authors of the present work consider optimal governance of DER in a model-free setting [11]. Additional recent strategies for DER control are cataloged in [12].

Due to the nonlinear nature of power flow equations, many OPFs are formulated as quadratically constrained quadratic programs (QCQPs). A popular method for analyzing such OPFs is relaxation via semidefinite programming (SDP) [13], [14]. It is well documented that relaxation of OPF problems via SDP often fails to achieve a rank-one solution [15], [16], [17].

As an example, in the work of [16] too many binding constraints will preclude convergence to a rank-one solution. The authors of [17] explored the extension of SDP to weakly meshed networks. Their technique was able to achieve a rank-one solution only after incorporating significant penalties on reactive power dispatch, effectively limiting the feasible region of control. Finally, in [14], the authors faced difficulty in obtaining a rank-one solution for certain network configurations.

In order to ameliorate these issues, the authors have previously explored the use of Extremum Seeking (or ES) to control active and reactive power injections of DER. Extremum Seeking is a nonlinear and model-free control technique that has been used to enable real time optimization in a variety of applications including robotic motion control [18] and solar PV maximum power point tracking (MPPT) [19]. The approach is model-free in the sense that the algorithm does not utilize any exogenous knowledge about the system over which it is optimizing in the decision-making process.

The ES scheme operates by perturbing the local action space and, subsequently, observing the effect of these perturbations in system outputs. From these observations, an input to output mapping (i.e. a gradient) is extracted that is used to determine proper actions at the next time instant. The process is repeated until the gradient being extracted, on average, becomes 0.

In the scheme, individual DER, each controlled by a separate ES controller, modulate their active and reactive power consumptions/injections sinusoidally. These sinusoids propagate through the network, affecting system voltages and power flows. Measurements are then collected from locations in the network where control authority is desired. From these measurements, a system-wide fitness function (essentially an OPF objective function) is computed and broadcast to all DER. Using this broadcast objective, which is a scalar value, the ES controllers can extract their respective gradients needed to perform optimization. Obviously, the speed of the approach is dependent on the rate at which data can be collected from points of interest in the network and the speed of objective function computation and broadcast. The overall scheme presents less of a burden from an implementation standpoint as it only requires measurements at points of the network where control action is desired, unlike centralized OPF approaches that require knowledge of all system loads. The ES approach has been successfully demonstrated in a power hardware in the loop environment in controlling real PV inverters for feeder voltage regulation [20].

Recently, we have explored the use of a 2-dimensional Extremum Seeking (2D-ES) algorithm to control the real and reactive power contributions of DER [11] in balanced electric power distribution systems. This approach successfully enabled DER active and reactive power injections to track substation active power and voltage targets while simultaneously regulating feeder voltages. The algorithm did not require the system topology, line segment impedances, or global knowledge of load behavior.

In this work, we extend the 2D-ES approach to regulate distribution voltage phase angles. Using this extension, we formulate a model-free optimization problem to virtually island a portion of a distribution network via modulating

## 2D-ES CONTROLLER NOMENCLATURE

$\Psi$	Objective function
$f_m$	$m^{th}$ 2D-ES probe frequency
$\omega_m$	$m^{th}$ 2D-ES probe angular frequency
$a_{u,m}$	$m^{th}$ 2D-ES probe amplitude for active power channel
$h_{u,m}$	$m^{th}$ 2D-ES high-pass filter frequency for active power channel
$l_{u,m}$	$m^{th}$ 2D-ES low-pass filter frequency for active power channel
$k_{u,m}$	$m^{th}$ 2D-ES integrator gain for active power channel
$\hat{u}_m$	$m^{th}$ 2D-ES active power setpoint
$u_m$	$m^{th}$ 2D-ES active power dispatch
$a_{v,m}$	$m^{th}$ 2D-ES probe amplitude for reactive power channel
$h_{v,m}$	$m^{th}$ 2D-ES high-pass filter frequency for reactive power channel
$l_{v,m}$	$m^{th}$ 2D-ES low-pass filter frequency for reactive power channel
$k_{v,m}$	$m^{th}$ 2D-ES integrator gain for reactive power channel
$\hat{v}_m$	$m^{th}$ 2D-ES reactive power setpoint
$v_m$	$m^{th}$ 2D-ES reactive power dispatch

DER power injections while simultaneously providing voltage regulation. Additionally, we provide a convergence proof of the 2D-ES scheme for optimizing convex objective functions in *unbalanced* (meshed and un-meshed) distribution networks.

This paper is organized as follows. In Section II, we provide an overview of the 2D-ES scheme as well as a convergence proof for unbalanced distribution grids. We present simulation results in Section III that show the ability of the approach to virtually island a portion of the network via regulating distribution voltage phasors. We then provide concluding remarks in Section IV.

## II. ANALYSIS

In this section, scalars are represented by plain letters. Vectors are represented by bold lowercase letters, and vectors that collect a set of similar scalars are represented by the bold lowercase letter of the scalar. Matrices are represented by bold uppercase letters. The notation  $\circ$  refers to the Hadamard (i.e entry-wise) product. The  $\text{diag}(\mathbf{x})$  operator returns a square matrix with the elements of  $\mathbf{x}$  on the diagonal, and zeros for all off-diagonal indices.

### A. Preliminaries

We begin with a discussion of the physics of a distribution network. Consider an unbalanced distribution network of arbitrary topology, where  $\mathcal{N}$  denotes the set of nodes, and  $\mathcal{L}$  denotes the set of lines that connect nodes. Kirchoff's Voltage Law (KVL) expressed for two adjacent nodes  $m$  and  $n$  connected by line  $(m, n)$  is:

$$[\mathbf{e}_m \circ \angle \boldsymbol{\delta}_m = \mathbf{e}_n \circ \angle \boldsymbol{\delta}_n + \mathbf{Z}_{mn} \mathbf{i}_{mn}]_{\mathcal{P}_{mn}}, \quad (1)$$

where  $\mathbf{e}_m = [e_m^a \angle 0, e_m^b \angle 0, e_m^c \angle 0]^T$  is the real vector of node voltage phasor magnitudes at node  $m$ ,  $\boldsymbol{\delta}_m = [\delta_m^a, \delta_m^b, \delta_m^c]^T$  is the vector of voltage phase angles at node  $m$ ,  $\mathbf{e}_m \circ \angle \boldsymbol{\delta}_m$  is the complex vector of voltage phasors at node  $m$  where  $\angle \boldsymbol{\delta}_m = [1 \angle \delta_m^a, 1 \angle \delta_m^b, 1 \angle \delta_m^c]^T \in \mathbb{C}^{3 \times 1}$ ,  $\mathbf{Z}_{mn}$  is the impedance matrix for line  $(m, n)$ ,  $\mathbf{i}_{mn} = [i_{mn}^a, i_{mn}^b, i_{mn}^c]^T$  is the vector of node current phasors on line  $(m, n)$  from node

$m$  to node  $n$ . The notation  $[\cdot]_{\mathcal{P}_{mn}}$  indexes the equation by the set of phases  $(\mathcal{P}_{mn})$  of line  $(m, n)$ , as in [14], [21]. It should be noted that  $\mathbf{e}_m^\phi = |\mathbf{e}_m^\phi \angle \delta_m^\phi|$  and  $\delta_m^\phi = \angle(\mathbf{e}_m^\phi \angle \delta_m^\phi)$  where the superscript  $\phi$  denotes an arbitrary phase.

Kirchoff's Current Law (KCL) for node  $m$  is written as:

$$\mathbf{i}_m + \sum_{n:(m,n) \in \mathcal{L}} [\mathbf{i}_{mn}]_{\mathcal{P}_{mn}} = 0, \quad (2)$$

where  $\mathbf{i}_m = [i_m^a, i_m^b, i_m^c]^T$  denotes the current entering node  $m$ . Taking the Hadamard Product of  $\mathbf{e}_m \circ \angle \delta_m$  with the complex conjugate of (2) and substituting for  $\mathbf{e}_m \circ \angle \delta_m$  by using (1) inside the summation, gives:

$$\mathbf{e}_m \circ \angle \delta_m \circ \mathbf{i}_m^* \dots + \sum_{n:(m,n) \in \mathcal{L}} [(\mathbf{e}_n \circ \angle \delta_n + \mathbf{Z}_{mn} \mathbf{i}_{mn}) \circ \mathbf{i}_{mn}^*]_{\mathcal{P}_{mn}} = 0. \quad (3)$$

This can be rewritten as in terms of loads, power injections, and line power flows as:

$$\mathbf{d}_m + \boldsymbol{\mu}_m + \sum_{n:(m,n) \in \mathcal{L}} [(\mathbf{s}_{mn} + \mathbf{l}_{mn})]_{\mathcal{P}_{mn}} = 0, \quad (4)$$

where  $\mathbf{d}_m = [d_m^a, d_m^b, d_m^c]^T$  is the vector of complex loads (including capacitors),  $\boldsymbol{\mu}_m = [\mu_m^a, \mu_m^b, \mu_m^c]^T$  is the vector of complex power injections (due to DER),  $\mathbf{s}_{mn} = [s_{mn}^a, s_{mn}^b, s_{mn}^c]^T$  is the vector of complex power phasors for line  $(m, n)$  entering node  $n$ , and  $\mathbf{l}_{mn} = [l_{mn}^a, l_{mn}^b, l_{mn}^c]^T$  is the vector of complex power losses on line  $(m, n)$ .

Finally, we can rewrite (1) by substituting line current with line power divided by node voltage:

$$[\mathbf{e}_m \circ \angle \delta_m = \mathbf{e}_n \circ \angle \delta_n + \mathbf{Z}_{mn} \mathbf{s}_{mn} \oslash (\mathbf{e}_n \circ \angle \delta_n)]_{\mathcal{P}_{mn}}, \quad (5)$$

where  $\oslash$  denotes Hadamard division (index-wise division). For a full discussion of how to explicitly define voltage phasor magnitude and voltage phasor angle from (4) and (5), the reader is invited to view [21].

For an unbalanced distribution network with  $N$  nodes and  $L$  line segments, let  $\mathbf{e}$  denote the collection of all voltage magnitudes,  $\boldsymbol{\delta}$  denote the collection of all voltage angles,  $\mathbf{p}$  denote the collection of all line segment active power flows, and  $\mathbf{q}$  the collection of all line segment reactive power flows, where entries of  $\mathbf{e}, \boldsymbol{\delta}, \mathbf{p}, \mathbf{q}$  corresponding to nonexistent phases, nodes, or lines are omitted:

$$\mathbf{e} = [e_1^a, e_2^a, \dots, e_N^a, e_1^b, e_2^b, \dots, e_N^b, e_1^c, e_2^c, \dots, e_N^c]^T, \quad (6)$$

$$\boldsymbol{\delta} = [\delta_1^a, \delta_2^a, \dots, \delta_N^a, \delta_1^b, \delta_2^b, \dots, \delta_N^b, \delta_1^c, \delta_2^c, \dots, \delta_N^c]^T, \quad (7)$$

$$\mathbf{p} = [p_1^a, p_2^a, \dots, p_L^a, p_1^b, p_2^b, \dots, p_L^b, p_1^c, p_2^c, \dots, p_L^c]^T, \quad (8)$$

$$\mathbf{q} = [q_1^a, q_2^a, \dots, q_L^a, q_1^b, q_2^b, \dots, q_L^b, q_1^c, q_2^c, \dots, q_L^c]^T. \quad (9)$$

Without loss of generality, consider  $C$  controllable DER capable of injecting or sinking both active and reactive power into the distribution grid. Let the vector  $\boldsymbol{\mu}$  represent the collection of all DER active ( $u$ ) and reactive ( $v$ ) power injections:

$$\boldsymbol{\mu} = [\mathbf{u}^T, \mathbf{v}^T]^T = [u_1, u_2, \dots, u_C, v_1, v_2, \dots, v_C]^T. \quad (10)$$

Lastly, let  $\mathbf{y}$  denote the collection of the aforementioned terms  $\mathbf{e}, \boldsymbol{\delta}, \mathbf{p}, \mathbf{q}, \mathbf{u}, \mathbf{v}$  as:

$$\mathbf{y} = [\mathbf{e}^T, \boldsymbol{\delta}^T, \mathbf{p}^T, \mathbf{q}^T, \mathbf{u}^T, \mathbf{v}^T]^T. \quad (11)$$

### B. Mapping from 2D-ES Power Injections to Network States

Let  $\mathbf{y} = \mathbf{f}(\boldsymbol{\mu})$  denote the nonlinear mapping from  $\boldsymbol{\mu} \rightarrow \mathbf{y}$  which can be constructed from (5) for all nodes  $m \in \mathcal{N}$  and (4) for all lines  $(m, n) \in \mathcal{L}$ . The mapping  $\mathbf{f}$  can be found by successively substituting rows of (4) and (5) into one another and collecting terms until the right-hand side of the system of equations contains only the elements of  $\boldsymbol{\mu}$ . As such, the mapping  $\mathbf{f}(\boldsymbol{\mu})$  captures all of the nonlinearities associated with 3 phase and unbalanced power flow. Note that we do not need to explicitly compute this mapping in the subsequent analysis. We make the assumption that such a vector mapping exists and that it is analytic in  $\boldsymbol{\mu}$ .

Without loss of generality, suppose the collection of 2D-ES controllers for a particular system are used to minimize a convex objective of the form:

$$\Psi = \frac{1}{2}(\mathbf{y} - \mathbf{y}^*)^T \mathbf{M}(\mathbf{y} - \mathbf{y}^*), \quad (12)$$

where  $\mathbf{M}$  is a symmetric positive semi-definite matrix (for  $\Psi$  to be convex) and  $\mathbf{y}^*$  is the optimal network state. The scalar function  $\Psi$  can represent system losses, deviation from a pre-defined voltage or power flow schedule, or a wide array of other objectives. We assume that this function is determined by an external entity (the distribution system operator, for instance). As  $\mathbf{f}$  is analytic in  $\boldsymbol{\mu}$ , we consider a first order Taylor expansion of  $(\mathbf{y} - \mathbf{y}^*)$  around the point  $\boldsymbol{\mu}^*$ , with  $\mathbf{y}^* = \mathbf{f}(\boldsymbol{\mu}^*)$ :

$$\mathbf{y} - \mathbf{y}^* = \mathbf{f}(\boldsymbol{\mu}) - \mathbf{f}(\boldsymbol{\mu}^*) \approx \mathbf{J}_{\boldsymbol{\mu}}(\boldsymbol{\mu}^*)(\boldsymbol{\mu} - \boldsymbol{\mu}^*), \quad (13)$$

where  $\mathbf{J}_{\boldsymbol{\mu}}$  is the Jacobian of  $\mathbf{f}$  (we assume this is full rank). Substituting (13) into (12) yields:

$$\begin{aligned} \Psi &= \frac{1}{2}(\boldsymbol{\mu} - \boldsymbol{\mu}^*)^T \underbrace{\mathbf{J}_{\boldsymbol{\mu}}(\boldsymbol{\mu}^*)^T \mathbf{M} \mathbf{J}_{\boldsymbol{\mu}}(\boldsymbol{\mu}^*)}_{\mathbf{B}} (\boldsymbol{\mu} - \boldsymbol{\mu}^*), \\ &= \frac{1}{2}(\boldsymbol{\mu} - \boldsymbol{\mu}^*)^T \mathbf{B}(\boldsymbol{\mu} - \boldsymbol{\mu}^*). \end{aligned} \quad (14)$$

The matrix  $\mathbf{B}$  is positive semi-definite and symmetric due to the full rank of  $\mathbf{J}_{\boldsymbol{\mu}}(\boldsymbol{\mu}^*)$ .

### C. Extremum Seeking Overview

Here we provide an overview of the two-dimensional *Extremum Seeking* approach that governs the active and reactive power contributions of individual DERs. A detailed analysis of the algorithm with a convergence proof for a convex objective function for unbalanced distribution systems is provided in Section II-D. There are many variations of ES algorithms, but the one considered here can be intuitively thought of as an approximate gradient-based descent process. For this type of extremum seeking, a small perturbation is injected into system input channels. This dither causes changes in the system states (voltage magnitudes and phase angles, and line active and reactive power flows). States at points in the system where

control is to be exercised are collected via sensors which, in turn, are used to compute the global objective function,  $\Psi$ . The present value of this scalar function is then broadcast to all 2D-ES controllers, each of which can then extract their “averaged” gradient to determine the proper active and reactive power to inject into the system at the next timestep.

A block diagram of the 2D-ES approach is shown for a single controller enclosed by the red dashed line in Fig. 1. The feedback controller consists of two loops, one of which governs active power injections and the other governing reactive power. Here, the objective function,  $\Psi(\mathbf{u}, \mathbf{v})$ , is a function of two independent vectors, where  $\mathbf{u}$  is the collection of DER active power injections and  $\mathbf{v}$  is the collection of DER reactive power injections. We refer to the quantities  $\mathbf{u}$  and  $\mathbf{v}$  as active and reactive power “dispatch”, that is, the active and reactive power that is injected into the system. The “Objective” block constitutes the mapping of active and reactive power injections to quantities measured by sensors in the distribution grid that are used to construct  $\Psi(\mathbf{u}, \mathbf{v})$ . Individual 2D-ES controllers, in this case, operate by injecting a sinusoidal perturbation of  $a_u \cos \omega t$  in the active power input channel, and  $a_v \sin \omega t$  in the reactive power input channel. These dither signals propagate throughout the distribution grid causing  $\Psi(\mathbf{u}, \mathbf{v})$  to have a D.C. component and an oscillatory component. Measurements of the objective function, which are broadcast to each 2D-ES controller, are passed through washout (high-pass) filters in both the active and reactive power loops. Following high-pass filtering, the resulting signal in each channel is demodulated with the same sinusoidal function and frequency as the dither (e.g.  $\cos \omega t$  in the active power loop and  $\sin \omega t$  in the reactive power loop). Then, the signal in each loop is passed through a low-pass filter, followed by an integrator with negative gain. We refer to the resulting signals,  $\hat{\mathbf{u}}$  and  $\hat{\mathbf{v}}$ , as active and reactive power “setpoints”. These setpoints are then summed with their respective dither signals and fed back into system (i.e. the objective function block). The signals  $\hat{\xi}_u$  and  $\hat{\xi}_v$  are estimates of the gradient of the objective function with respect to  $\mathbf{u}$  and  $\mathbf{v}$ .

An illustration of multiple DER managed by individual  $n$  2D-ES controllers optimizing a common objective is also presented in Fig. 1. As is shown in the figure, the 2D-ES controllers operate in parallel, each of which manages a different component of the input vectors  $\mathbf{u}$  and  $\mathbf{v}$ . All 2D-ES controllers utilize the same scalar input signal,  $\Psi(\mathbf{u}, \mathbf{v})$ . The theory of extremum seeking, as discussed in [22], guarantees convergence of  $(\mathbf{u}, \mathbf{v})$  to a region around the optimum  $(\mathbf{u}^*, \mathbf{v}^*)$  provided “unique” frequencies are chosen for each of the 2D-ES blocks, where it must be ensured that:  $\omega_i \neq \omega_j$  and  $\omega_i + \omega_j \neq \omega_k$  for distinct  $i, j$ , and  $k$ . This will prevent the different 2D-ES controllers from interfering with one another when extracting their respective gradients [22].

#### D. Stability Analysis

We now show that the collection of  $n$  2D-ES controllers operating in parallel (as depicted in Fig. 1) will minimize (14). To begin, let  $\hat{\boldsymbol{\mu}}$  denote the vector of active power and reactive power setpoints of all 2D-ES controllers as in (15), let  $\mathbf{A}$

denote a square matrix with probe amplitudes on the diagonal as in (16), and let  $\mathbf{r}(t)$  represent a time varying vector of probe sinusoids as in (17):

$$\hat{\boldsymbol{\mu}} = [\hat{\mathbf{u}}^T, \hat{\mathbf{v}}^T]^T = [\hat{u}_1, \hat{u}_2, \dots, \hat{u}_C, \hat{v}_1, \hat{v}_2, \dots, \hat{v}_C]^T. \quad (15)$$

$$\mathbf{A} = \text{diag} \left( [a_{u,1}, \dots, a_{u,C}, a_{v,1}, \dots, a_{v,C}]^T \right), \quad (16)$$

$$\mathbf{r}(t) = [\cos \omega_1 t, \cos \omega_2 t, \dots, \cos \omega_C t, \sin \omega_1 t, \sin \omega_2 t, \dots, \sin \omega_C t]^T. \quad (17)$$

Let  $\boldsymbol{\rho}$  denote the vector of the outputs of the 2D-ES controller high-pass filter outputs as in (18),  $\boldsymbol{\epsilon}$  denote the vector of difference between the objective function and the outputs of the 2D-ES controller high-pass filters as in (19), and  $\boldsymbol{\xi}$  denote the vector of the outputs of the 2D-ES controller low-pass filters as in (20).

$$\boldsymbol{\rho} = [\rho_{u,1}, \rho_{u,2}, \dots, \rho_{u,C}, \rho_{v,1}, \rho_{v,2}, \dots, \rho_{v,C}]^T, \quad (18)$$

$$\boldsymbol{\epsilon} = [\epsilon_{u,1}, \epsilon_{u,2}, \dots, \epsilon_{u,C}, \epsilon_{v,1}, \epsilon_{v,2}, \dots, \epsilon_{v,C}]^T, \quad (19)$$

$$\boldsymbol{\xi} = [\xi_{u,1}, \xi_{u,2}, \dots, \xi_{u,C}, \xi_{v,1}, \xi_{v,2}, \dots, \xi_{v,C}]^T. \quad (20)$$

Let  $\mathbf{H}$  denote a diagonal matrix of high-pass filter cutoff frequencies as in (21),  $\mathbf{L}$  denote the diagonal matrix of low-pass filter cutoff frequencies as in (22),  $\mathbf{K}$  denote the diagonal matrix of 2D-ES controller integrator gains as in (23), and  $\mathbf{1}$  denote the vector with all entries being 1 as in (24).

$$\mathbf{H} = \text{diag} \left( [h_{u,1}, \dots, h_{u,C}, h_{v,1}, \dots, h_{v,C}]^T \right), \quad (21)$$

$$\mathbf{L} = \text{diag} \left( [l_{u,1}, \dots, l_{u,C}, l_{v,1}, \dots, l_{v,C}]^T \right), \quad (22)$$

$$\mathbf{K} = \text{diag} \left( [k_{u,1}, \dots, k_{u,C}, k_{v,1}, \dots, k_{v,C}]^T \right), \quad (23)$$

$$\mathbf{1} = [1, 1, \dots, 1]^T \in \mathbb{R}^{2C \times 1}, \quad (24)$$

As in Fig. 1, the active power, and reactive power, injections of the  $m^{\text{th}}$  2D-ES controller are:

$$\begin{aligned} u_m &= \hat{u}_m + a_{u,m} \cos \omega_m t, \\ v_m &= \hat{v}_m + a_{v,m} \sin \omega_m t. \end{aligned} \quad (25)$$

With (10) and (15) – (17) all 2D-ES controller active and reactive power injections, can be expressed compactly ((25) for all  $m \in \{1, 2, \dots, C\}$ ) as:

$$\mathbf{u} = \hat{\boldsymbol{\mu}} + \mathbf{A} \mathbf{r}(t). \quad (26)$$

In Fig. 1,  $\boldsymbol{\rho}$  represents the high frequency content of the objective function  $\Psi$ , which can be thought of as how  $\Psi$  is changing with respect to the sinusoidal probes. The variable  $\boldsymbol{\epsilon}$  (not shown in Fig. 1) represents the low frequency content of the objective function  $\Psi$ , which can be thought of as how  $\Psi$  is changing with respect to the setpoint,  $\hat{\boldsymbol{\mu}}$ , as defined in (27):

$$\boldsymbol{\epsilon} = \Psi(\boldsymbol{\mu}, \mathbf{r}(t)) \cdot \mathbf{1} - \boldsymbol{\rho}. \quad (27)$$

We introduce the shifted set of coordinates:

$$\tilde{\boldsymbol{\mu}} = \hat{\boldsymbol{\mu}} - \boldsymbol{\mu}^*, \quad (28)$$

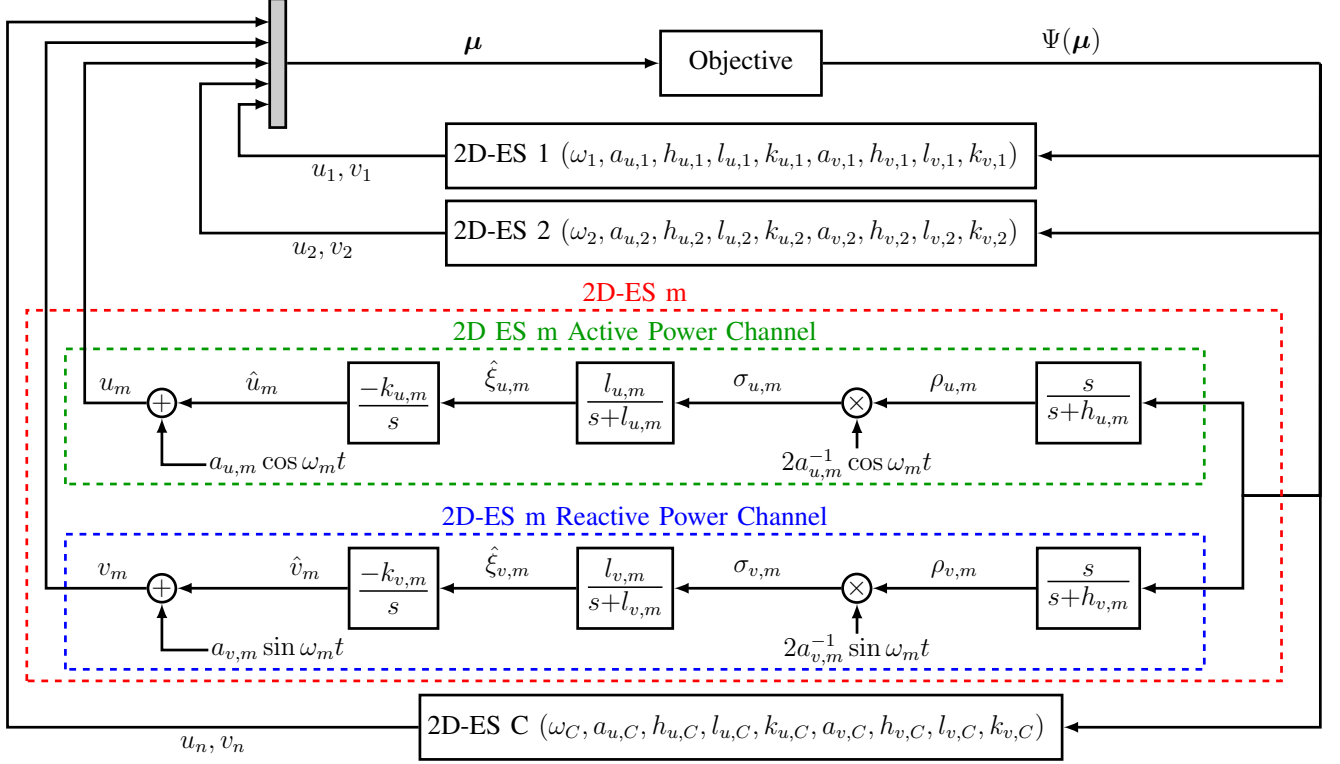


Fig. 1: Parallel operation of multiple 2D-ES controllers.

and rewrite the objective function (14) in terms of new shifted coordinate and the perturbation signals as (29):

$$\begin{aligned}
 \Psi &= \frac{1}{2}(\mu - \mu^*)^T B(\mu - \mu^*), \\
 &= \frac{1}{2}(\hat{\mu} + Ar - \mu^*)^T B(\hat{\mu} + Ar - \mu^*), \\
 &= \frac{1}{2}(\tilde{\mu} + Ar)^T B(\tilde{\mu} + Ar), \\
 &= \frac{1}{2}\tilde{\mu}^T B\tilde{\mu} + r^T(t)A^T B\tilde{\mu} + \frac{1}{2}r^T(t)A^T BAr(t).
 \end{aligned} \tag{29}$$

In light of (28), (29) and Fig. 1, the dynamics of the collection of 2D-ES controllers minimizing (29) can be expressed as:

$$\dot{\epsilon} = H(\Psi(\tilde{\mu}, r(t)) \cdot \mathbf{1} - \epsilon), \tag{30}$$

$$\dot{\xi} = 2A^{-1}Lr(t) \circ (\Psi(\tilde{\mu}, r(t)) \cdot \mathbf{1} - \epsilon) - L\xi, \tag{31}$$

$$\dot{\tilde{\mu}} = -K\xi. \tag{32}$$

Let  $\bar{\tau}$  be the lowest common multiple of all probe time periods in the system,  $\tau_m = f_m^{-1}$ , in the system such that the entire system is  $\bar{\tau}$ -periodic,  $\bar{\tau} = \gamma_m \tau_m$ ,  $\gamma_m \in \mathbb{Z}^+ \setminus 0$ . The angular frequency of the dither of the  $m^{th}$  2D-BES controller is:  $\omega_m = \gamma_m \bar{\omega}$  where  $\bar{\omega} = 2\pi\bar{\tau}^{-1}$ . We introduce the new timescale of  $\tau = t\bar{\tau}^{-1}$ , and rewrite (30) – (32) as:

$$\dot{\epsilon} = \bar{\tau}H(\Psi(\tilde{\mu}, r(\tau)) \cdot \mathbf{1} - \epsilon), \tag{33}$$

$$\dot{\xi} = \bar{\tau}(2LA^{-1}r(\tau) \circ (\Psi(\mu, r(\tau)) \cdot \mathbf{1} - \epsilon) - L\xi), \tag{34}$$

$$\dot{\tilde{\mu}} = -\bar{\tau}K\xi, \tag{35}$$

where the dot notation on the left-hand side of (33) – (35) now refers to  $d/d\tau$ , and all variables are functions of  $\tau$ . The

system of equations (33) – (35) represent the 2D-ES dynamics of (30) – (32) in the new timescale over the period  $\bar{\tau}$ . This system is in the form to which averaging is applicable, and we integrate over the period 0 to  $\bar{\tau}$ , to obtain the “averaged” system dynamics of (36) – (38):

$$\dot{\epsilon}_{av} = H \left( \left( \frac{1}{2}\tilde{\mu}_{av}^T B\tilde{\mu}_{av} + \frac{1}{4}\text{Tr}(A^T B A) \right) \cdot \mathbf{1} - \epsilon_{av} \right) \tag{36}$$

$$\dot{\xi}_{av} = L(B\tilde{\mu}_{av} - \xi_{av}) \tag{37}$$

$$\dot{\tilde{\mu}}_{av} = -K\xi_{av}, \tag{38}$$

where in computing (36) - (38), the following relations were utilized:

$$rr^T = \frac{1}{2} \begin{bmatrix} I_{C \times C} + Y_{C \times C} & X_{C \times C} \\ X_{C \times C} & I_{C \times C} + Z_{C \times C} \end{bmatrix}, \tag{39}$$

$$X(m, n) = \sin((\gamma_m + \gamma_n)\bar{\omega}\tau) + \sin((\gamma_m - \gamma_n)\bar{\omega}\tau), \tag{40}$$

$$Y(m, m) = \cos(2\gamma_m \bar{\omega}\tau), \tag{41}$$

$$Y(m, n) = \cos((\gamma_m - \gamma_n)\bar{\omega}\tau) + \cos((\gamma_m + \gamma_n)\bar{\omega}\tau), \tag{42}$$

$$Z(m, m) = -\cos(2\gamma_m \bar{\omega}\tau), \tag{43}$$

$$Z(m, n) = \cos((\gamma_m - \gamma_n)t) - \cos((\gamma_m + \gamma_n)\bar{\omega}\tau), \tag{44}$$

for all  $m, n \in \{1, \dots, C\}$ . In the system of (36) - (38), the subscript “av” refers to:  $1/T \int_0^T (\cdot) d\tau$  and  $T = \bar{\tau}$ . The system of equations (36) – (38) represent the averaged 2D-ES dynamics of (33) – (35) over the period of  $\tau$ . Recognizing that (37) - (38) evolve independently of (36), we proceed in analyzing

the sub-system consisting of (37) - (38). This sub-system can be re-organized into the linear system:

$$\begin{bmatrix} \dot{\xi}_{av} \\ \dot{\tilde{\mu}}_{av} \end{bmatrix} = \underbrace{\begin{bmatrix} -L & LB \\ -K & 0 \end{bmatrix}}_{\Omega} \begin{bmatrix} \xi_{av} \\ \mu_{av} \end{bmatrix}. \quad (45)$$

In order to prove the average system dynamics of (45) are stable, consider the following Lyapunov function, (46):

$$V = \frac{1}{2} [\xi_{av} \quad \tilde{\mu}_{av}] P \begin{bmatrix} \xi_{av} \\ \tilde{\mu}_{av} \end{bmatrix}, \quad (46)$$

where  $P$  is positive definite and symmetric. We seek to find a pair of positive definite matrices  $(P, Q)$  that satisfy the Lyapunov equation:  $\Omega^T P + P \Omega = -Q$ . Consider the matrices:

$$P = \begin{bmatrix} \Lambda & -L^{-1} \\ -L^{-1} & K^{-1}(I + \Lambda LB) \end{bmatrix}, \quad (47)$$

$$Q = \begin{bmatrix} L\Lambda - KL^{-1} & 0 \\ 0 & B \end{bmatrix}, \quad (48)$$

where  $\Lambda \succ 0$  is a diagonal matrix. If  $\Lambda \succ KL^{-2} \succ 0$ , then it can be shown that  $P$  is positive definite and  $Q$  is positive semi-definite (due to the positive semi-definiteness of  $B$ ). This implies (45) is stable. To establish asymptotic stability, we note that  $\dot{V}$  is of the form:

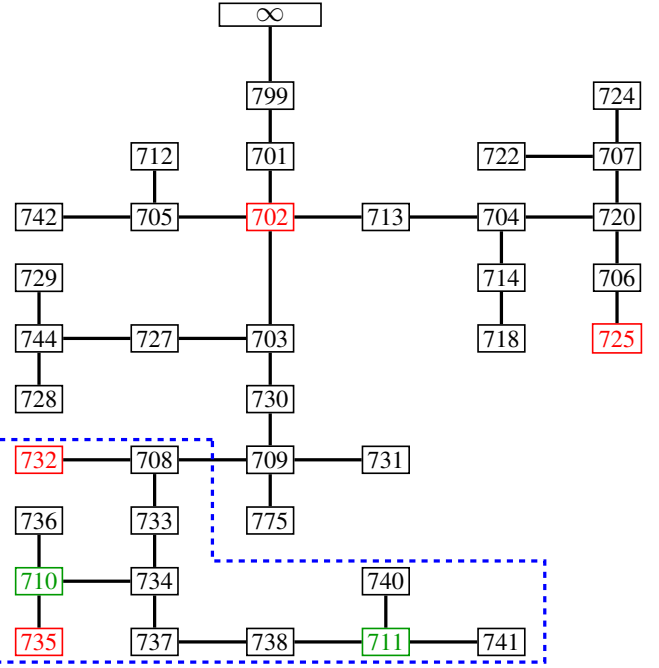
$$\dot{V} \leq -\tilde{\mu}_{av}^T B \tilde{\mu}_{av}, \quad (49)$$

which is negative definite outside of the equilibrium set. This implies that the 2D-ES control scheme will asymptotically drive  $\tilde{\mu}_{av}$  to the equilibrium set  $\{\tilde{\mu}_{av,eq} | \tilde{\mu}_{av,eq}^T B \tilde{\mu}_{av,eq} = 0\}$ . Convergence of  $\tilde{\mu}$  to a region near of  $\mu^*$  is then guaranteed by the averaging process and proper choice of parameters of the 2D-ES control loops [22], [11].

Returning to (36), which is a vector of the averaged DC content of the objective function value for each loop in all 2D-ES controllers, we see that  $\epsilon_{av} \rightarrow \frac{1}{4} \text{Tr}(A^T B A) \cdot \mathbf{1}$ . This term is typically negligible as  $A$  is diagonal and its elements consist of the perturbation amplitudes of each 2D-ES loop, this term is typically negligible as  $(a_{u,m}, a_{v,m}) \ll 1$ .

#### E. Role of the PMU

The analysis of Section II-D shows optimizing convex functions of  $e$ ,  $\delta$ ,  $p$ , or  $q$  using the 2D-ES method will result in convergence to a small neighborhood of the optimum, without explicit knowledge of the system model. This result makes the proposed approach applicable to a wide range of potential objective functions. In this work, we exploit the availability of voltage phase angle measurements,  $\delta$ , to enable virtual islanding based on controlling voltage magnitude and phase angle alone. It is true that the previous analysis allows for direct control of  $p$  and  $q$ , however, in the 2D-ES scheme, this would require that the active and reactive power flows between portions of the feeder to be virtually islanded be explicitly measured. This, in turn, would require the deployment of current transformers to capture measurements needed to compute



power measurements on the line, the difference in voltage magnitude and difference in voltage angle can serve as a proxy measurement, as the the line power phasor and difference in voltage phasors are directly related. While not a linear relationship, driving one to zero is approximately equivalent to driving the other to zero, and vice-versa. Assuming three phase measurements of the voltage magnitude and voltage angle at nodes 709 and 708 are available, one can minimize the line power by minimizing the difference in voltage magnitude and difference in voltage angle.

We perform simulations on a modified version of the IEEE 37 node test feeder model, as shown in Fig. 2. Feeder topology, line configuration, line impedance, line length, and spot loads are specified in [23]. The voltage regulator between nodes 799 and 701 was omitted. The transformer between nodes 709 and 775, was replaced by a line of configuration 724 (according to [23], page 5) and length of 50 feet. All loads on both networks were assumed to be Wye connected and follow a ZIP model with a time varying element:

$$d_m^\phi(\boldsymbol{\mu}, t) = \underline{d}_m^\phi (1 + \kappa_m^\phi \sin(2\pi(\tau_m^\phi)^{-1}t)) \dots \times \left( A_{PQ,m}^\phi + A_{I,m}^\phi e_m^\phi(\boldsymbol{\mu}) + A_{Z,m}^\phi (e_m^\phi(\boldsymbol{\mu}))^2 \right), \quad (50)$$

where  $\underline{d}_m^\phi$  is the complex load specified in [23],  $A_{PQ,m}^\phi = 0.75$ ,  $A_{I,m}^\phi = 0.1$ ,  $A_{Z,m}^\phi = 0.15 \forall \phi \in \{a, b, c\}, \forall m \in \mathcal{N}$ ,  $\kappa_m^\phi \sim \mathcal{U}(-0.2, 0.2)$ , and  $\tau_m^\phi \sim \mathcal{U}(30, 480) \forall \phi \in \{a, b, c\} \forall m \in \mathcal{N}$ . We placed a PV plant at node 710 that injects 0.02 p.u. of active power on all three phases, and a PV plant at node 711 that injects 0.03 p.u. of active power on all three phases. The transmission line was treated as an infinite bus, with a fixed voltage reference of  $\mathbf{V}_\infty = [1, 1\angle 240^\circ, 1\angle 120^\circ]^T$  p.u.

Single-phase four quadrant capable DER were placed on all phases at nodes  $\{702, 725, 732, 735\}$ . We assumed each DER can inject or sink both active power and reactive power on its respective phase independently of other phases at the same node. DER were constrained by an apparent power capacity limit,  $\bar{w}_m$ , as listed in Table I. DER were also constrained by maximum, and minimum, reactive power limits of of  $0.8\bar{w}_m$ , and  $-0.8\bar{w}_m$ , respectively.

DER active power and reactive power dispatch were controlled by individual 2D-ES loops as in Fig. 1. Parameters for all controllers are listed in Table I. For each 2D-ES controller, the active power and reactive power probes had same probe frequency, high-pass filter frequency, low-pass filter frequency, integrator gain, and probe amplitude, and we therefore omit the subscript indicating the active power or reactive probe in Table I and this section. Controller probe frequency is listed in Table I as  $f_m$ , with angular frequency  $\omega_m = 2\pi f_m$ . The cutoff frequency of the high-pass filters was  $h_{u,m} = h_{v,m} = h_m = \omega_m/10$  and the cutoff frequency of the low-pass filers was  $l_{u,m} = l_{v,m} = l_m = \omega_m/10$ . Probe frequencies must be unique,  $f_k \neq f_l \forall k, l \in \mathcal{C}$ , and non-additive,  $f_k + f_l \neq f_m \forall k, l, m \in \mathcal{C}$ . We therefore chose probe frequencies as  $f = \sqrt{b}/[\sqrt{b}]$  where  $b$  is a prime number and  $b \geq 11$ . This algorithm was effective in producing frequencies,  $f_m \in [1, 1.25]$ , that satisfy the uniqueness and non-additive conditions for  $11 \leq b \leq 1000$ .

**TABLE I:** ES controller parameters. Subscripts  $u$  and  $v$  that denote the active and reactive power channels are omitted as we assign the same parameters to the active and reactive power control loops.

Node	Phase	$f_m$ (Hz)	$a_m$ (p.u.)	$k_m$	$\bar{w}_m$ (p.u.)
702	a	$\sqrt{11}/3$	0.0025	0.25	0.100
	b	$\sqrt{13}/3$	0.0025	0.25	0.095
	c	$\sqrt{17}/4$	0.0025	0.25	0.090
725	a	$\sqrt{19}/4$	0.0025	0.25	0.050
	b	$\sqrt{23}/4$	0.0025	0.25	0.045
	c	$\sqrt{29}/5$	0.0025	0.25	0.040
732	a	$\sqrt{31}/5$	0.0025	0.25	0.070
	b	$\sqrt{37}/6$	0.0025	0.25	0.080
	c	$\sqrt{41}/6$	0.0025	0.25	0.075
735	a	$\sqrt{43}/6$	0.0025	0.25	0.075
	b	$\sqrt{47}/6$	0.0025	0.25	0.070
	c	$\sqrt{53}/7$	0.0025	0.25	0.080

DER setpoints computed by the 2D-ES controllers were adjusted to ensure the sinusoidal probe plus the setpoint always remained feasible with respect to DER complex power constraints (see [24] for a detailed description of this process).

In the simulations, every 2D-ES controller has knowledge of its own parameters, including the probe frequency, probe amplitude, high-pass filter cutoff frequency, low-pass filter cutoff frequency, and integrator gain. Every 2D-ES controller also receives measurements of the objective function at each timestep in the simulation. All 2D-ES controller has knowledge of their own internal states, their own complex power setpoints, and their own complex power dispatch, as shown in Fig. 1. We assume each 2D-ES controller has knowledge of DER active power capacity, reactive power capacity, and apparent power capacity. The 2D-ES controllers have no knowledge pertaining to the network, other than the objective function measurements. Finally, the 2D-ES controllers have no knowledge pertaining to other ES controllers (e.g. the controllers do not exchange information).

The objective of this experiment was to minimize the voltage phasor difference across the line between nodes 709 and 708, by minimizing (51):

$$\begin{aligned} \Psi(\boldsymbol{\mu}) = & \alpha_e \sum_{\phi \in \{a, b, c\}} \left( (e_{709}^\phi(\boldsymbol{\mu}))^2 - (e_{708}^\phi(\boldsymbol{\mu}))^2 \right)^2 \dots \\ & + \alpha_\delta \sum_{\phi \in \{a, b, c\}} \left( \delta_{709}^\phi(\boldsymbol{\mu}) - \delta_{708}^\phi(\boldsymbol{\mu}) \right)^2 \dots \\ & + \alpha_{emax} \sum_{\substack{m \in \mathcal{N} \setminus \infty \\ \phi \in \{a, b, c\}}} \left( \max(e_m^\phi(\boldsymbol{\mu}) - 1.05, 0) \right)^2 \dots \\ & + \alpha_{emin} \sum_{\substack{m \in \mathcal{N} \setminus \infty \\ \phi \in \{a, b, c\}}} \left( \max(0.95 - e_m^\phi(\boldsymbol{\mu}), 0) \right)^2, \end{aligned} \quad (51)$$

where  $\mathcal{N}$  is the set of all nodes, and coefficients of  $\alpha_e = 10^5$ ,  $\alpha_\delta = 10^6$ , and  $\alpha_{emin} = \alpha_{emax} = 10^2$  were chosen to scale each part of the objective function on the order of 1. The last two lines of (51) represent voltage magnitude regulation and will enforce proper voltage magnitudes throughout the simulation.

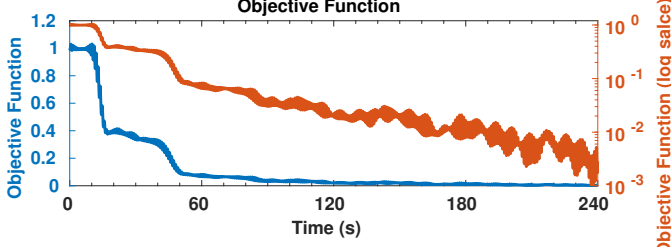


**Fig. 3:** Value of the objective function, defined in (51), normalized by its value at  $t = 0$ .

Fig. 3 plots the objective function over time in both normal and logarithmic scales, where the objective function has been normalized by its value at  $t = 0$ . It is evident that the objective function (51) is minimized by the DER dispatch managed by the 2D-ES controllers.

Fig. 4 plots the voltage magnitude for nodes 709 and 708, and Fig. 5 plots the per phase voltage magnitude difference across line (709, 708), with the per phase voltage magnitude difference defined as  $e_{709}^\phi(\mu) - e_{708}^\phi(\mu)$ .

Fig. 6 plots the voltage angle for nodes 709 and 708, and Fig. 7 plots the per phase voltage angle difference across line (709, 708) over time, with the per phase voltage angle difference defined as:

$$\delta_{709}^\phi(\mu) - \delta_{708}^\phi(\mu) = \frac{180^\circ}{\pi} (\angle V_{709}^\phi(\mu) - \angle V_{708}^\phi(\mu)).$$

Figs. 3 – 6 highlight the effectiveness of ES control in minimizing both the magnitude and phase angle differences. The thickness of the lines in these plots show the implication of the sinusoidal perturbation signals, which are always present in the system.

Fig. 8a plots the active power on line (709, 708),  $P_{709,708}^\phi(\mu)$ , Fig. 8b plots the reactive power on line (709, 708),  $Q_{709,708}^\phi(\mu)$ , and Fig. 8c plots the apparent power on line (709, 708),  $S_{709,708}^\phi(\mu)$ . Fig. 8 clearly demonstrates that minimizing the voltage phasor difference across a line minimizes the active and reactive power flow across the line. The effect of the dither signal is also clearly visible in Fig. 8 as the “average” active power, reactive power, and apparent power are driven toward zero, however the actual active power, and reactive power, remain within a neighborhood of the optimum value.

Fig. 8c plots the total apparent power on line (709, 708). The apparent power is driven toward zero as the voltage magnitude and voltage angle are also driven toward zero. The “average” apparent power decreases from 0.237 p.u. at the beginning of the simulation to 0.011 p.u. at the end. This corresponds to a 95% reduction from 590 kVAr to 28 kVAr, based on the feeder power rating.

Fig. 9, Fig. 10, Fig. 11, and Fig. 12, plot the evolution of the complex power setpoints and complex power dispatch the 2D-ES controllers at nodes 702, 725, 732, and 735, respectively. All 2D-ES controllers have zero initial setpoints and dispatch. Fig. 12 depicts the saturation of the DER on phase  $c$  at node 735, where the control is constrained at times by the maximum

reactive power limit, and at times by the maximum apparent power limit.

### B. Importance of Voltage Angle Control

As a final note, we want to discuss the implications of being able to control the voltage phase angle for virtual islanding. We performed a second simulation with two scenarios. In the first scenario, the 2D-ES controllers solely minimize voltage magnitude difference, by minimizing (51) with  $\alpha_e = 10^5$ ,  $\alpha_\delta = 0$ ,  $\alpha_{emin} = \alpha_{emax} = 10^2$ , without any constraints on DER. In the second scenario, the 2D-ES controllers minimize voltage magnitude difference and voltage angle difference, by minimizing (51) with  $\alpha_e = 10^5$ ,  $\alpha_\delta = 10^6$ ,  $\alpha_{emin} = \alpha_{emax} = 10^2$ , without any constraints on DER. The results of these two scenarios are shown in Fig. 13 that depicts a drastic difference in performance between minimizing only voltage magnitude difference, and minimizing both voltage magnitude difference and voltage angle difference, on line apparent power. The “average” optimal apparent power for first scenario (no minimization of voltage angle difference) is 0.081 p.u., or 203 kVAr, and the “average” optimal apparent power at the end of the second scenario (minimization of both voltage magnitude difference and voltage angle difference) is 0.006 p.u., or 15 kVAr, corresponding to a 92 % reduction in line apparent power.

## IV. CONCLUSIONS

This paper considered the application of two-dimensional Extremum Seeking (2D-ES) control to manage the active and reactive power outputs of DER in electric power distribution systems. Building on earlier work, here we extended the convergence proof of the 2D-ES scheme to *unbalanced* (both meshed and unmeshed) distribution systems. When optimizing a convex function of distribution grid voltages, phase angles, active and reactive power line flows, the proof shows convergence of the system to a small neighborhood of the optimizer. The generality of the proof allows a large variety of different OPF objective functions to be optimized using the 2D-ES scheme.

Using the newly derived result, we developed a model-free optimization approach to virtually island different portions of a distribution network using 2D-ES driven DER. We argued that the availability of the voltage phase angle provided by distribution PMUs allows one to approximatley island portions of the distribution network *without knowledge of the system model and without having to measure power flows across the portion of the network to be islanded*.

Virtual islanding is a special case of the more general objective, to drive a voltage phasor at a particular node on a distribution circuit to a desired value by recruiting DER. For example, our approach could enable more routine circuit reconfigurations for reasons of voltage management or loss minimization. Furthermore, voltage phasors could be used to control or limit power flow on a specific circuit section, e.g. to prevent reverse power flow or voltage violations on a feeder. Our group is investigating these broader use cases and algorithms for phasor-based control.

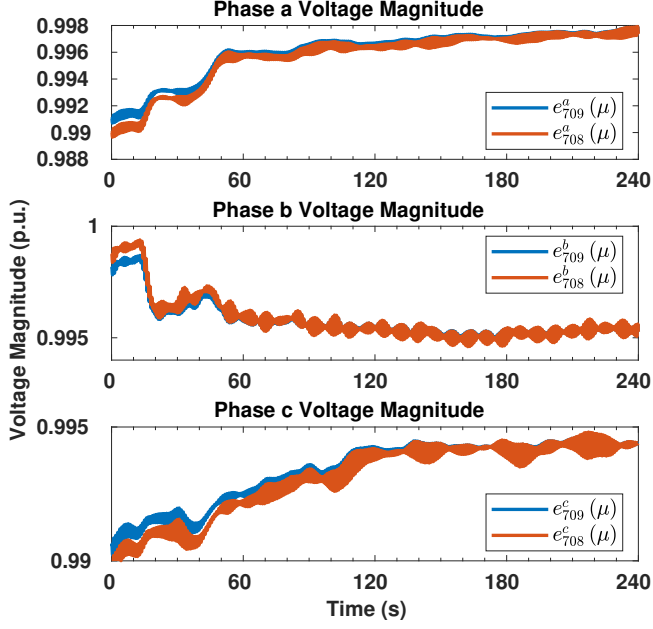


Fig. 4: Voltage magnitude at nodes 709 and 708.

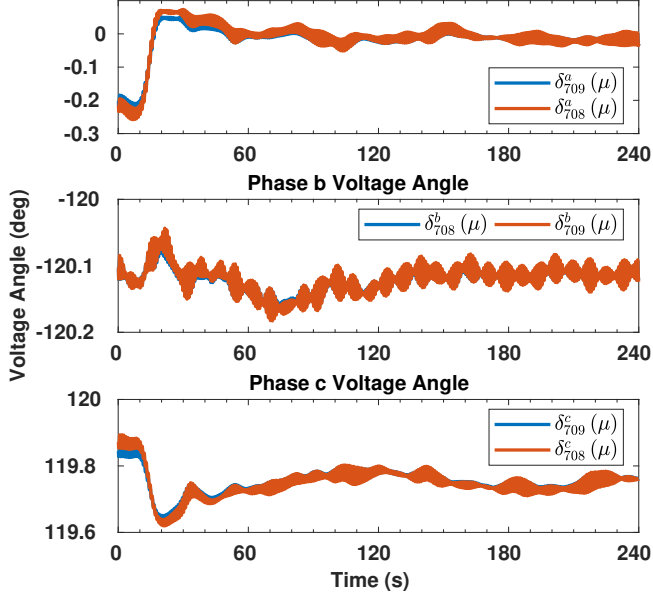
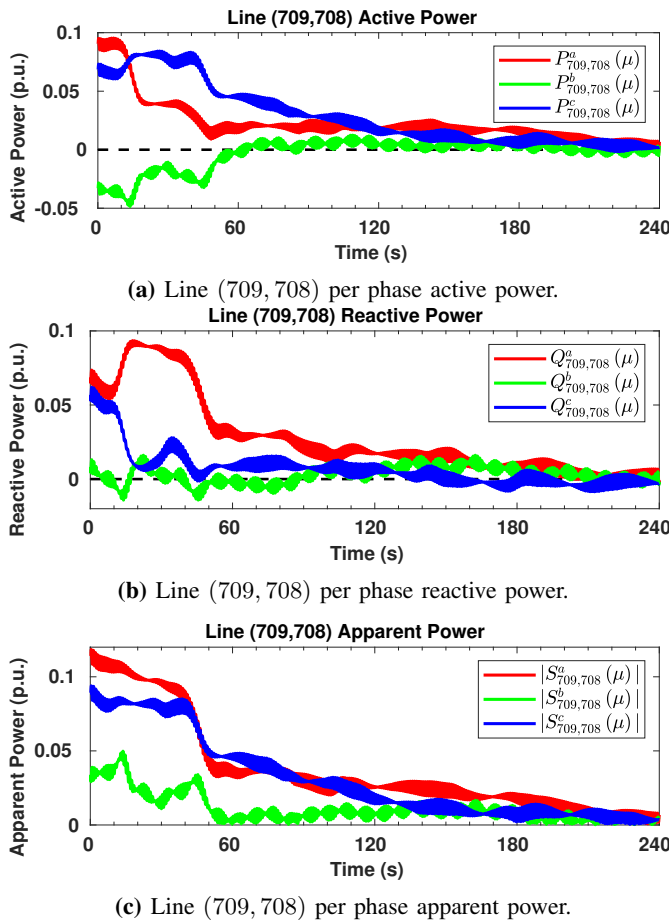


Fig. 6: Voltage angle at nodes 709 and 708.

In a previous work, we studied the stability of ES with an exponential decay in probe amplitude [24]. Incorporation of the probe amplitude decay algorithm into this work would ameliorate the dither in voltage magnitude and voltage angle difference, and enable such values to remain within tighter bounds from their optimal values.

## REFERENCES

- [1] A. Von Meier, E. Stewart, A. McEachern, M. Andersen, and L. Mehrmanesh, "Precision micro-synchrophasors for distribution systems: A summary of applications," *IEEE Trans. Smart Grid*, vol. 8, no. 6, pp. 2926–2936, 2017.
- [2] "Synchrophasor fact sheet," accessed, June-2010. [Online]. Available: [https://cdn.selinc.com/assets/Literature/Product%20Literature/Flyers/FS\\_Synchrophasor\\_BF\\_20100617.pdf?v=20150408-131001](https://cdn.selinc.com/assets/Literature/Product%20Literature/Flyers/FS_Synchrophasor_BF_20100617.pdf?v=20150408-131001)
- [3] "SEL-351 protection system data sheet," accessed, July-2019. [Online]. Available: [https://cdn.selinc.com/assets/Literature/Product%20Literature/Data%20Sheets/351-5-6-7\\_PS\\_DS\\_20190111.pdf?v=20190327-194137](https://cdn.selinc.com/assets/Literature/Product%20Literature/Data%20Sheets/351-5-6-7_PS_DS_20190111.pdf?v=20190327-194137)
- [4] "SPAU 140C synchro-check relay, product guide," accessed July 2019. [Online]. Available: [https://library.e.abb.com/public/8bbfb5b573eb0ae36c1257176002994de/spau140c\\_tob\\_750421enc.pdf](https://library.e.abb.com/public/8bbfb5b573eb0ae36c1257176002994de/spau140c_tob_750421enc.pdf)
- [5] L. F. Ochoa and D. H. Wilson, "Angle constraint active management of distribution networks with wind power," in *2010 IEEE PES Innovative Smart Grid Technologies Conference Europe (ISGT Europe)*. IEEE, 2010, pp. 1–5.
- [6] D. Wang, D. Wilson, S. Venkata, and G. C. Murphy, "PMU-based angle constraint active management on 33kV distribution network," in *22nd Int. Conf. Elect. Distribution*. IET, 2013, pp. 1–4.
- [7] Q. Shafiee, J. M. Guerrero, and J. C. Vasquez, "Distributed secondary control for islanded microgrids—a novel approach," *IEEE Trans. Power Electron.*, vol. 29, no. 2, pp. 1018–1031, 2013.
- [8] F. Katiraei, M. R. Iravani, and P. W. Lehn, "Micro-grid autonomous



**Fig. 8:** Line (709, 708) per phase active power, reactive power, and apparent power. Phase  $a$  is plotted in red, phase  $b$  is plotted in blue, and phase  $c$  is plotted in green.

operation during and subsequent to islanding process,” *IEEE Trans. Power Del.*, vol. 20, no. 1, pp. 248–257, 2005.

- [9] Y. Zhang, M. Hong, E. Dall’Anese, S. V. Dhople, and Z. Xu, “Distributed controllers seeking AC optimal power flow solutions using ADMM,” *IEEE Trans. Smart Grid*, vol. 9, no. 5, pp. 4525–4537, 2017.
- [10] Y. Xu, Z. Y. Dong, R. Zhang, and D. J. Hill, “Multi-timescale co-ordinated voltage/var control of high renewable-penetrated distribution systems,” *IEEE Trans. Power Syst.*, vol. 32, no. 6, pp. 4398–4408, 2017.
- [11] D. B. Arnold, M. D. Sankur, M. Negrete-Pincetic, and D. Callaway, “Model-free optimal coordination of distributed energy resources for provisioning transmission-level services,” *IEEE Trans. Power Syst.*, vol. 33, no. 1, pp. 817–829, Jan. 2018.
- [12] K. E. Antoniadou-Plytaria, I. N. Kouveliotis-Lysikatos, P. S. Georgilakis, and N. D. Hatziargyriou, “Distributed and decentralized voltage control of smart distribution networks: Models, methods, and future research,” *IEEE Trans. Smart Grid*, vol. 8, no. 6, pp. 2999–3008, Nov. 2017.
- [13] E. Dall’Anese, G. B. Giannakis, and B. F. Wollenberg, “Optimization of unbalanced power distribution networks via semidefinite relaxation,” in *North Amer. Power Symp. (NAPS)*. IEEE, 2012, pp. 1–6.
- [14] E. Dall’Anese, H. Zhu, and G. Giannakis, “Distributed optimal power flow for smart microgrids,” *IEEE Trans. Smart Grid*, vol. 4, no. 3, pp. 1464–1475, Sept. 2013.
- [15] B. C. Lesieutre, D. K. Molzahn, A. R. Borden, and C. L. DeMarco, “Examining the limits of the application of semidefinite programming to power flow problems,” in *Communication, Control, and Computing (Allerton), 2011 49th Annual Allerton Conference on*. IEEE, 2011, pp. 1492–1499.
- [16] R. Louca, P. Seiler, and E. Bitar, “Nondegeneracy and inexactness of semidefinite relaxations of optimal power flow,” *arXiv preprint arXiv:1411.4663*, 2014.
- [17] R. Madani, S. Sojoudi, and J. Lavaei, “Convex relaxation for optimal

power flow problem: Mesh networks,” *IEEE Trans. Power Syst.*, vol. 30, no. 1, pp. 199–211, Jan. 2015.

- [18] C. Zhang, D. Arnold, N. Ghods, A. Siranossian, and M. Krstic, “Source seeking with non-holonomic unicycle without position measurement and with tuning of forward velocity,” *Systems & control letters*, vol. 56, no. 3, pp. 245–252, 2007.
- [19] S. J. Moura and Y. A. Chang, “Lyapunov-based switched extremum seeking for photovoltaic power maximization,” *Control Engineering Practice*, vol. 21, no. 7, pp. 971–980, 2013.
- [20] J. Johnson, S. Gonzalez, and D. B. Arnold, “Experimental distribution circuit voltage regulation using DER power factor, volt-var, and extremum seeking control methods,” in *2017 IEEE 44th Photovoltaic Specialist Conference (PVSC)*. IEEE, 2017, pp. 3002–3007.
- [21] M. Sankur, “Optimal control of commercial office battery systems, and grid integrated energy resources on distribution networks,” Ph.D. dissertation, UC Berkeley, 2017.
- [22] K. B. Ariyur and M. Krstic, *Real-time optimization by extremum-seeking control*. John Wiley & Sons, 2003.
- [23] “IEEE distribution test feeders,” accessed May-2015. [Online]. Available: <http://ewh.ieee.org/soc/pes/dsacom/testfeeders/index.html>
- [24] M. Sankur and D. Arnold, “Extremum seeking control of distributed energy resources with decaying dither and equilibrium-based switching,” in *Proceedings of the 52nd Hawaii International Conference on System Sciences*, 2019.



**Michael D. Sankur** is a computational project scientist in the Grid Integration Group at Lawrence Berkeley National Laboratory. He received a B.S. in Mechanical Engineering in 2008, and an M.S. in Engineering Science in 2009, both from the University of California, San Diego. He received a Ph.D. from the Mechanical Engineering Dept. at the University of California, Berkeley in 2017, and afterwards worked as a postdoctoral researcher with the Grid Integration Group at LBNL. Currently, his research focuses on novel implementations of model-free control and optimization techniques and applications for electric grid resiliency and cyber security.



**Roel Dobbe** is a Postdoctoral Researcher with the AI Now Institute at New York University. He received a BSc in Mechanical Engineering and a MSc in Systems & Control from the TU Delft, the Netherlands, and a PhD in Control, Intelligent Systems & Energy from the Department of Electrical Engineering and Computer Sciences at UC Berkeley. His research addresses the development, analysis, integration and governance of data-driven systems. His PhD work combined optimization, machine learning and control theory to enable monitoring and control of safety-critical systems, including energy & power systems and cancer diagnosis and treatment. His recent work revisits notions of safety in the design of data-driven systems to incorporate perspectives from law, policy and social sciences. He works on the translation between engineering, computer science and policy, including issues of algorithmic accountability in practice and the role of transparency in stakeholder engagement for building safe and trustworthy algorithmic systems.



**Alexandra “Sascha” von Meier** (M’10) is an adjunct professor in the Department of Electrical Engineering and Computer Science at the University of California, Berkeley and directs the Electric Grid Research program at the California Institute for Energy and Environment (CIEE). She is also a faculty scientist at the Lawrence Berkeley National Laboratory. Her research is driven by the vision of a nimble, adaptable and resilient electric power infrastructure that optimally recruits intermittent renewable resources, energy storage and electric demand response. She holds a B.A. in Physics (1986) and a Ph.D. in Energy and Resources (1995) from UC Berkeley.

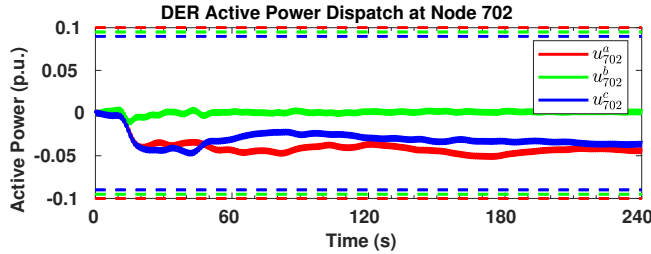


Fig. 9: Node 702 active power and reactive power dispatch. Dashed lines represent DER power dispatch limits for the corresponding phase.

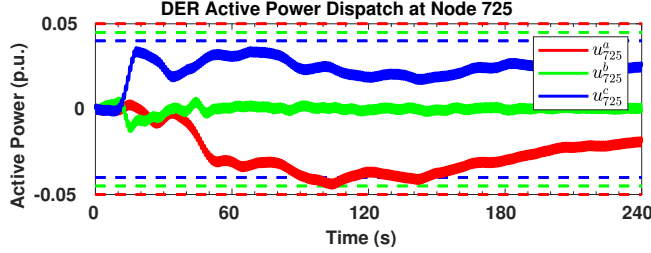
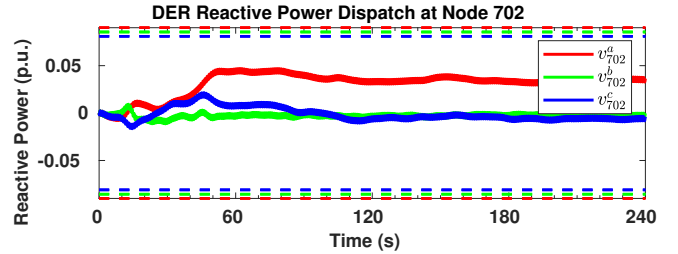


Fig. 10: Node 725 active power and reactive power dispatch. Dashed lines represent DER power dispatch limits for the corresponding phase.

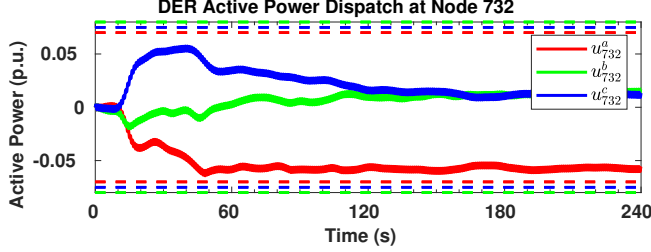
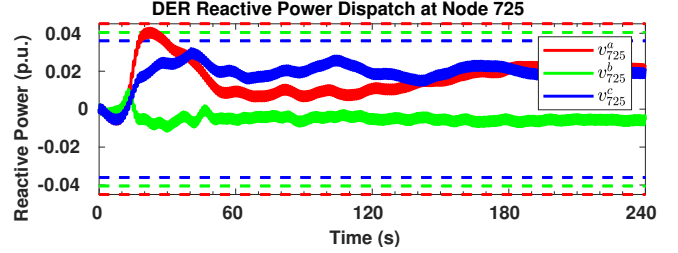


Fig. 11: Node 732 active power and reactive power dispatch. Dashed lines represent DER power dispatch limits for the corresponding phase.

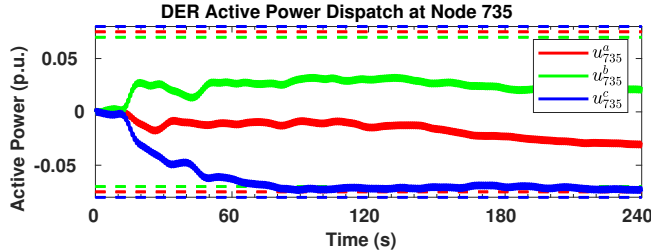
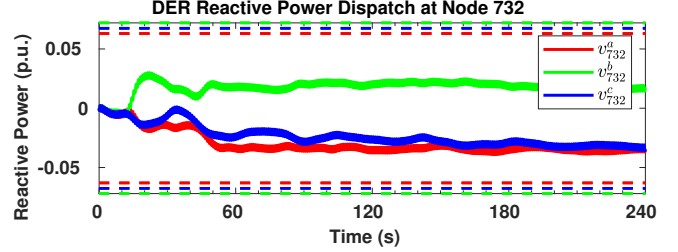
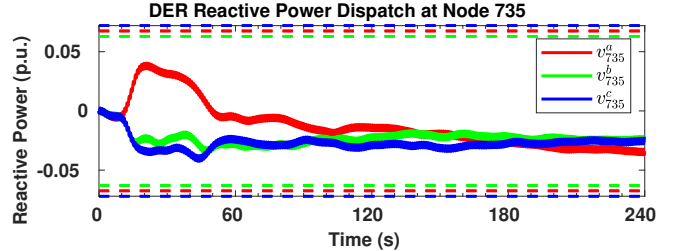


Fig. 12: Node 735 active power and reactive power dispatch. Dashed lines represent DER power dispatch limits for the corresponding phase.



**Daniel B. Arnold** is a research scientist in the Grid Integration Group at Lawrence Berkeley National Laboratory. He received the B.S. degree in Mechanical Engineering from the University of California, San Diego, in 2005, the M.S. degree in Engineering Science from the University of California, San Diego, in 2006. From 2006 to 2009 he conducted research and development of unmanned underwater vehicles for the United States Navy at the Space and Naval Warfare Center in San Diego, California. He then received his Ph.D. from the Mechanical

Engineering Dept. at the University of California, Berkeley in 2015. He was a 2015 ITRI-Rosenfeld Postdoctoral Fellow at the Lawrence Berkeley National Laboratory. Presently, his research focuses on the application of control, optimization, and machine learning techniques for electric grid resiliency and cyber security.

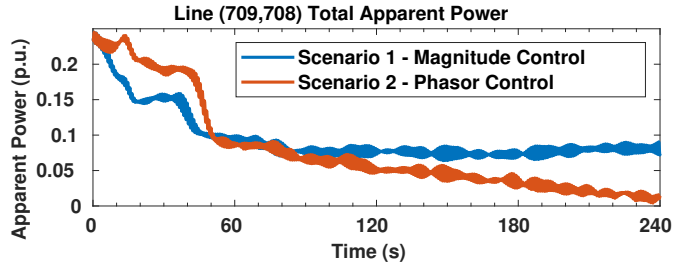


Fig. 13: Comparison of line (709,708) apparent power for scenario with no angle control (Scenario 1 - Magnitude Control), and scenario with angle control (Scenario 2 - Phasor Control).